

Article

# Trace Element Geochemistry of Magnetite: Implications for Ore Genesis of the Huanggangliang Sn-Fe Deposit, Inner Mongolia, Northeastern China

Cheng Wang <sup>1,2</sup>, Yongjun Shao <sup>1,2</sup>, Xiong Zhang <sup>3</sup>, Jeffrey Dick <sup>1,2</sup>  and Zhongfa Liu <sup>1,2,\*</sup>

<sup>1</sup> Key Laboratory of Metallogenic Prediction of Non-Ferrous Metals and Geological Environment Monitoring (Central South University), Ministry of Education, Changsha 410083, China; csuwangcheng@csu.edu.cn (C.W.); shaoyongjun@126.com (Y.S.); jeff@chnosz.net (J.D.)

<sup>2</sup> School of Geosciences and Info-Physics, Central South University, Changsha 410083, China

<sup>3</sup> 416 Geological Team, Bureau of Geology and Mineral Exploration and Development of Hunan Province, Zhuzhou 412007, China; dirtybear@163.com

\* Correspondence: liuzf61521@csu.edu.cn; Tel.: +86-731-888-30616

Received: 29 December 2017; Accepted: 17 April 2018; Published: 4 May 2018



**Abstract:** The Huanggangliang deposit is a super-large Sn-Fe deposit in the Huanggangliang–Ganzhuermiao metallogenic belt in the southern section of the Great Hinggan Range. The Sn-Fe deposits mainly occur in the skarn contact zone and were formed via the interaction of biotite-bearing alkali feldspar granite with limestone strata of the Permian Dashizhai and Zhesi Formations. Based on the intersecting relations among the ore-bearing veins and the different types of mineral assemblages within these veins, the Sn-Fe mineralization could be divided into two periods and four stages: the skarn period, which includes the garnet–diopside–magnetite (T1) stage (stage 1) and epidote–idocrase–cassiterite–magnetite (T2) stage (stage 2); and the quartz–magnetite period, which can be divided into the quartz–cassiterite–magnetite (T3) stage (stage 3) and quartz–magnetite (T4) stage (stage 4). In this paper, we discuss the genesis of magnetite, controlling factors for magnetite compositions, and type of ore genesis based on petrographic studies and LA-ICP-MS analyses of trace elements in these four types of magnetite from the Huanggangliang Sn-Fe deposit. The results demonstrate that the four types of magnetite are generally depleted in Ti (0.002–3.030 wt %), Al (0.008–1.731 wt %), and Zr (<1.610 ppm). In addition, the low Ni and Cr contents and relatively high and stable Fe contents in the four types of magnetite are indicative of hydrothermal genetic features. Compositions of the ore fluids and host rocks, formation of coexisting minerals, and other physical and chemical parameters (such as  $fO_2$ ) may have influenced the variable magnetite geochemistry in the different Huanggangliang ore types, with fluid compositions and  $fO_2$  probably playing the most important roles. The geological, petrographic, and geochemical characteristics of magnetite of the Huanggangliang Sn-Fe deposit lead us to conclude that the deposit is a skarn-type Sn-Fe deposit associated with Yanshanian medium-acidic magmatic activities.

**Keywords:** Huanggangliang Sn-Fe deposit; magnetite; trace elements; Huanggangliang–Ganzhuermiao metallogenic belt

## 1. Introduction

The southern segment of the Great Hingan Range constitutes part of the eastern section of the Central Asian Orogenic Belt (Xingmeng Orogenic Belt) (Figure 1A). The southern segment of the Great Hingan Range is separated from the northern margin of the North China block by the Xilamulun fracture zone. It is bordered by the Erenhot–Hegenshan fracture zone to the north and by the Nenjiang fracture zone to the east (Figure 1B). The southern segment of the Great Hingan Range is a

famous nonferrous metal base and Pb-Zn-W-Mo-Sn-Fe polymetallic ore concentration area in northern China [1,2]. The Huanggangliang–Ganzhuermiao metallogenic belt is in the center of the southern segment of the Great Hingan Range. It is a polymetallic metallogenic belt characterized by the largest number of deposits, largest scale, and richest mineral types in the southern segment of the Great Hingan Range [1–4]. Plenty of well-known deposits occur along the Huanggangliang–Ganzhuermiao fracture zone (Figure 1C), including the Haobugao Pb-Zn-Cu-Sn skarn deposit, the Baiyinnuoer Pb-Zn-Ag skarn deposit, the Dajing Cu-Sn magmatic-hydrothermal vein type deposit, the Aonaodaba Cu-Sn-Ag magmatic-hydrothermal vein type deposit, the Anle Sn-Cu magmatic-hydrothermal vein type deposit, and the Huanggangliang Sn-Fe deposit.

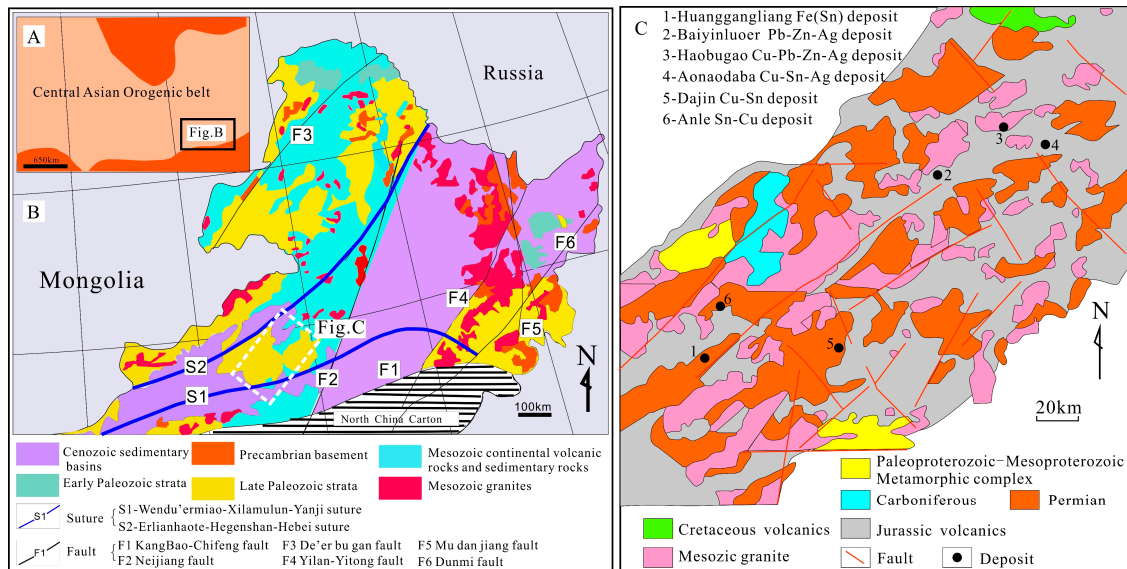


**Figure 1.** Geological sketch map and distribution of deposits in central Inner Mongolia, adjacent areas (A,B) and the southern segment of the Great Hingan Range (C), modified from Reference [3].

The Huanggangliang deposit is a super-large Sn-Fe deposit in the Huanggangliang–Ganzhuermiao metallogenic belt. Previous studies have concentrated on the geochronology, geochemistry [5–9], and geological features of the ore deposit [10,11] as well as the mineralogical features [7,12–16], timing of mineralization [7,9,17,18], fluid inclusion compositions [7,19,20], isotopic geochemistry [20–22], and ore-controlling factors of the granitic bodies associated with mineralization [23]. The following topics on the mineralization and genesis of the Huanggangliang Sn-Fe deposit are still under debate: (1) What are the relations between the Cretaceous k-feldspar granitic magma, Permian Dashizhai group and Zhesi group limestone contact metasomatism, and the formation of the skarn Sn-Fe deposit [3,6,7,9,14,19,20,22,24,25]? (2) The metallogensis of the deposit is characterized by a two-period metallogenic model of superimposition between the Permian sedimentary-exhalative process and the Yanshanian magmatic hydrothermal process. How does this model fit with the submarine hydrothermal exhalative-sedimentary series related to the Paleozoic volcanic-sedimentary basin evolution [21,26,27]? (3) Important submarine hydrothermal sedimentary-exhalative metallogensis did occur during the Permian sedimentary basin evolution process, and Yanshanian tectonic-magmatic activities also contributed to the formation of the deposit. The formation of the deposit experienced composite metallogensis with superimposition of the Permian exhalative-sedimentary process and the Yanshanian magmatic hydrothermal process [18].

Magnetite commonly exists in magmatic-type deposits and hydrothermal-type deposits as an accessory mineral within igneous, sedimentary, and metamorphic rocks [28–31], Magnetite has a typical spinel structure [30,32] and is compatible with trace elements—such as Mg, Al, Ti, V, Cr, Mn, Co, Ni, Zn, and Ga—within its structure [28,31]. Previous studies proposed that the structure and

composition of the magnetite are sensitive to the physical and chemical conditions present during its formation [28,29,32–38]. Recently, breakthroughs have been achieved in discriminating deposit genesis based on the structure and trace element composition of the magnetite [28,29,31,39].

Laser ablation inductively coupled plasma mass spectrometry (LA-ICP-MS) has been proven to be a powerful tool for defining the separate generation events of magnetite and hydrothermal mineralization [40–42]. However, no equivalent research has been conducted for the Huanggangliang Sn-Fe deposits. In this paper, we report the results obtained from LA-ICP-MS analyses on magnetites from the Huanggangliang Sn-Fe deposit for the first time and discuss pyrite genesis and physical and chemical conditions to present a new understanding of ore deposit types.

## 2. Regional Geology

The Great Hingan Range is in the strong transition zone between the NE-striking Paleozoic Asian tectono-metallogenic province and the NNE-striking Mesozoic–Cenozoic of the west Pacific Marginal tectono-metallogenic province (Figure 1).

The Huanggangliang–Ganzhuermiao metallogenic belt in the main part of the southern section of the Great Hingan Range is outcrops mainly within different strata units such as the Lower Proterozoic Baoyintu Group; the Lower Paleozoic Wenduermiao and Bainaimiao Groups; the Carboniferous Benbatu and Amushan Formations; the Permian Dashizhai, Huanggangliang, and Linxi Formations; the Jurassic Hongqi, Wanbao, Xinmin, and Manketouebo Formations; the Cretaceous Manitu, Baiyingaolao, and Meiletu Formation; and deposits of the Quaternary [3]. The folds include the Huanggangliang–Ganzhuermiao anticlinorium, the Lindong synclinorium, and the Tianshan anticlinorium. These fold belts constitute the NE-striking basic tectonic framework of the Late Hercynian [4,21]. The Yanshanian structures are dominated by fractures. Deep fault systems have been formed along the axis of the Late Hercynian anticlinorium, forming a belt with a series of NE-striking fracture-intrusive rocks and a fracture-volcanic rock belt. Magmatic activities are well-developed in the area, dominated by Yanshanian granitoids, and have a few Late Hercynian rock bodies [3]. The Yanshanian intrusions include biotite-bearing alkali feldspar granite and monzogranite. The Late Hercynian intrusions mainly include diorite and granodiorite, with occasional ultrabasic-basic stocks [4].

## 3. Ore Deposit Geology

The Huanggangliang deposit of Inner Mongolia is in the NW wing of the Huanggangliang anticlinorium (Figure 2A). From old to new strata, the exposed strata include sandstone and slate of the Lower Permian Qingfengshan Formation; andesite, spilite and keratophyre, tuff, and other volcanic rocks of the Dashizhai Formation; marble, sandstone, and shale of the Zhesi Formation; and slate and sandstone of the Upper Permian Linxi Formation (Figure 2A). The marbles of the Dashizhai Formation and the Zhesi Formation are the major ore-bearing strata in this area. Intrusive rocks of this area include the Early Cretaceous alkali granite and biotite-bearing alkali granites (Figure 2A), which are all distributed in the western part of the deposit area, with an outcrop length of approximately 15.4 km and a width of 1.5–2.0 km.

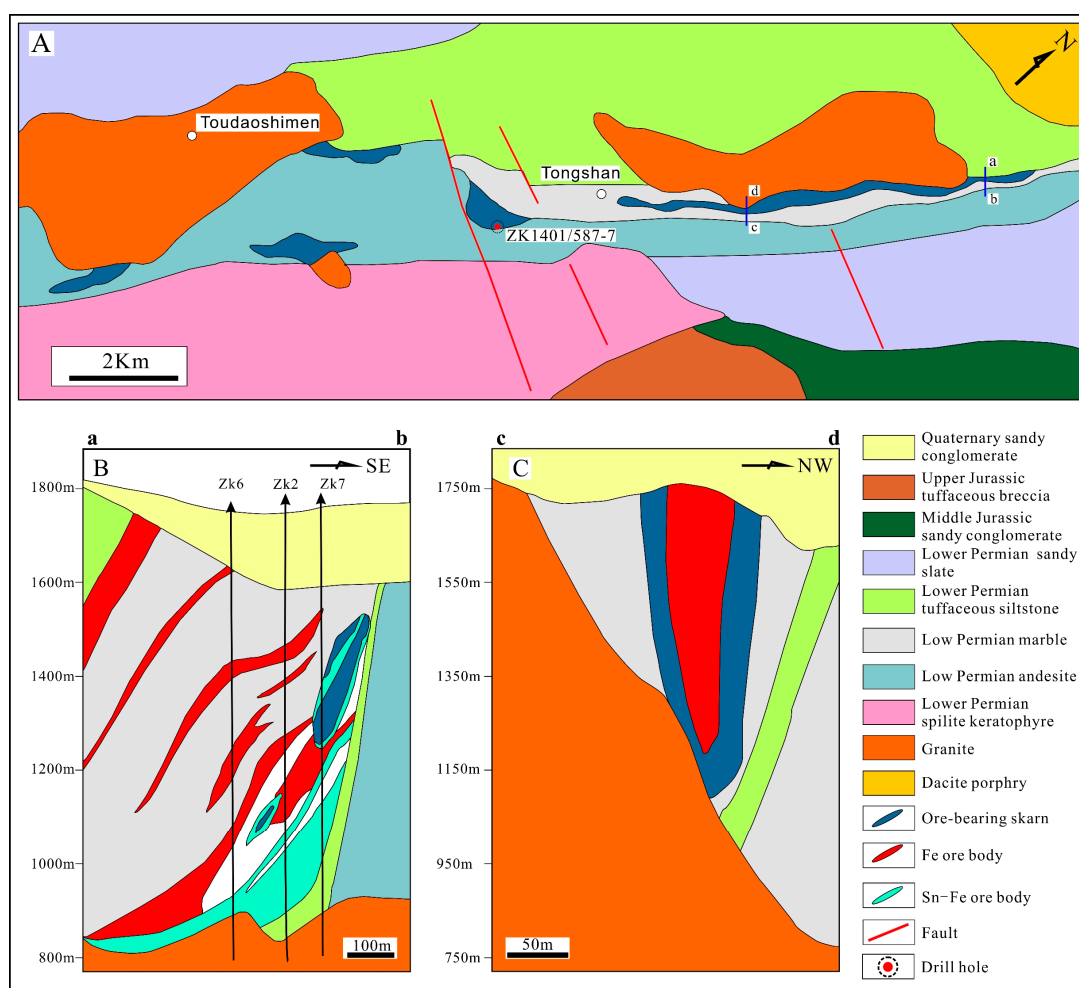


**Figure 2.** Simplified geological map (A) and cross sections (B,C) of the Huanggangliang Sn-Fe deposit. Modified from Reference [17].

The Huanggangliang orebodies occur within the contact zone between the Yanshanian alkali granite and the volcanoclastic rocks of the Permian Dashizhai Formation or the carbonate rock strata of the Zhesi Formation. The ore bodies exhibit stratiform, lenticular, and saddle shapes. Near the contact areas between the granite intrusion and the marble, the ore bodies show great thickness, good continuity, and high grades (Figure 2B,C). A Fe ore body and Sn-Fe ore body are the two major orebodies of the area (Figure 2B,C). Sn is found associated with Fe ores, and constitutes the most important associated mineral within the deposit. The Sn contents within the Fe ore bodies are below industrial grade (<0.2%). The Sn content within the Sn-Fe ore body is much higher (Sn grade reaches 0.20–3.74%). Sn-Fe ore bodies are observed to cut through Fe ore body (Figure 2B,C). Metallic minerals in the ores include magnetite, cassiterite, sphalerite, and galena. Non-metallic minerals include garnet, diopside, epidote, actinolite, gokumite, ivaite, chlorite, hastingsite, quartz, fluorite, calcite, and biotite. Ore textures include idiomorphic-hypidiomorphic granular texture, xenomorphic granular texture, and solid solution separation texture (Figure 3). Ore structures include both disseminated and massive structures. Wall rock alterations are well-developed and include silicified alteration, hornfelsic alteration, skarn alteration, fluoritization alteration, and carbonatization alteration, which are developed in the inner and outer contact zone between the Yanshanian alkali granite and the Permian strata [16,20].

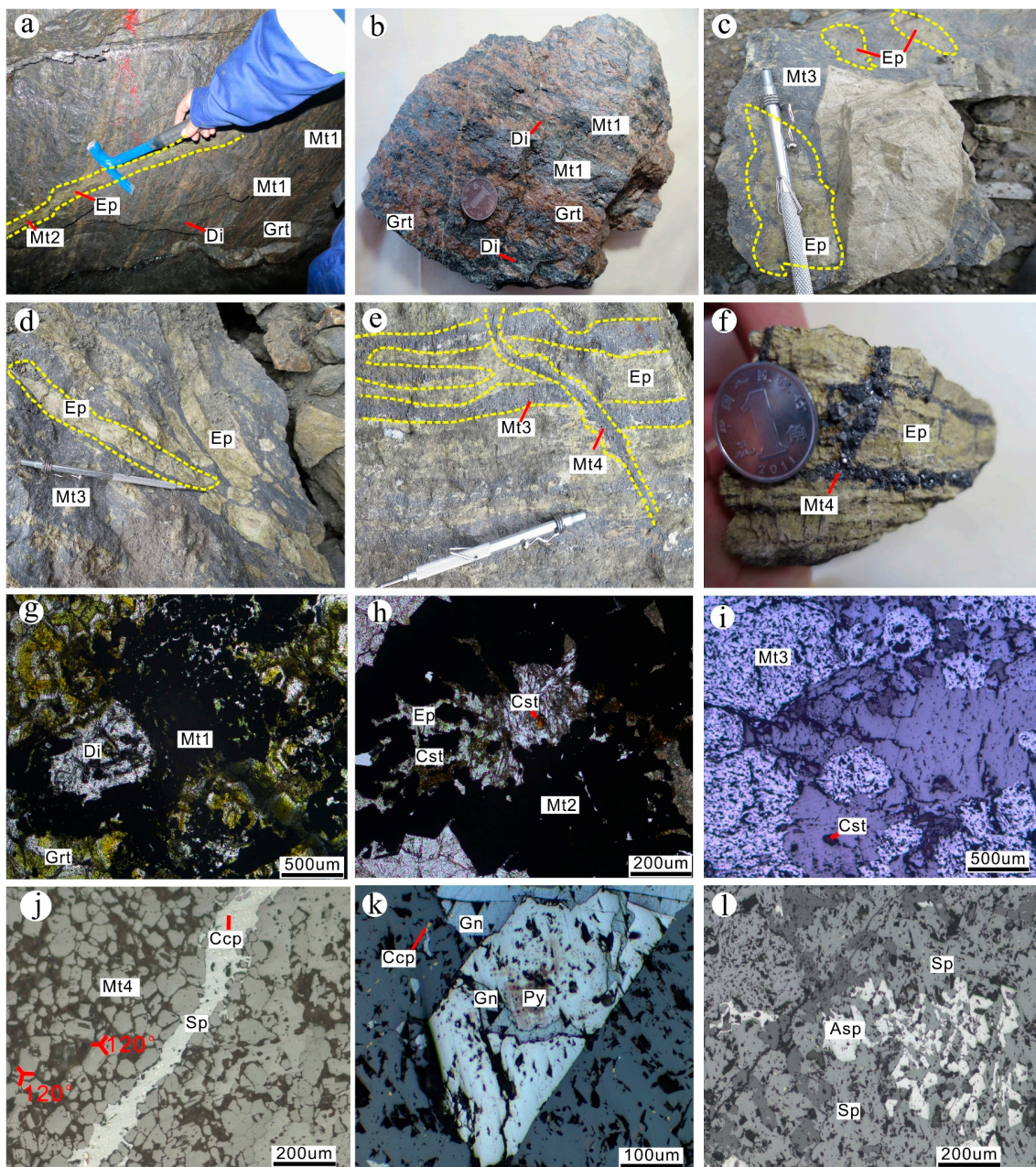


**Figure 3.** Mineral assemblages of the Huanggangliang Sn-Fe deposit. (a) Epidote skarn vein bearing disseminated magnetite (Mt2) cutting through banded garnet–diopside–magnetite (Mt1) ore body; (b) banded garnet–diopside–magnetite (Mt1) ore; (c) fine-grain massive magnetite (Mt3) cements epidote skarn bearing disseminated magnetite (Mt2); (d) fine-grain magnetite (Mt3) cements epidote skarn lenticles bearing disseminated magnetite (Mt2); (e) coarse-grain massive magnetite cutting through epidote skarn bearing disseminated magnetite (Mt2) which is cemented by fine-grain massive magnetite (Mt3); (f) coarse-grain massive magnetite vein (Mt4) cutting through epidote skarn containing disseminated magnetite; (g) xenomorphic magnetite replacing garnet and diopside, and later replaced by cassiterite; (h) xenomorphic magnetite replacing epidote and later replaced by cassiterite; (i) cassiterite, magnetite, and quartz assemblage; (j) magnetite occurring with idiomorphic texture, with inter-granule angles of  $120^\circ$ , showing typical triple junction texture. Intersection and cutting of later chalcopyrite–sphalerite; (k) galena replacing hypidiomorphic pyrite; (l) sphalerite replacing arsenopyrite. Grt—garnet; Di—diopside; Ep—epidote; Mt—magnetite; Cst—cassiterite; Ccp—chalcopyrite; Sp—sphalerite; Gn—galena; Py—pyrite; Asp—arsenopyrite.

Based on comprehensive studies of the intersection relations among the ore-bearing veins of the deposit and mineral assemblages of different types of ore-bearing veins (Figure 3a–f), the Sn-Fe metallogenesis can be divided into two periods and 4 stages (Figure 4). The skarn period can be subdivided into the garnet–diopside–magnetite (T1) stage (stage 1) and the epidote–idocrase–cassiterite–magnetite (T2) stage (stage 2). The quartz-magnetite period can be subdivided into the quartz–cassiterite–magnetite (T3) stage (stage 3) and the quartz-magnetite (T4) stage (stage 4). (1) The garnet–diopside–magnetite stage is dominated by the formation of skarn minerals—such as wollastonite, diopside, and garnet—with the occurrence of magnetites. Banded magnetite and sparsely disseminated magnetite are the major ore types; (2) In the epidote–idocrase–cassiterite–magnetite stage, a large amount of skarn minerals occurs, such as epidote, idocrase, hastingsite, and actinolite (Figure 3h). The ores have a densely disseminated structure; (3) In the quartz–cassiterite–magnetite stage, large amounts of hypidiomorphic magnetites occur, forming high-grade iron ores that cross-cut the skarn (Figure 3c,d). The ores have a massive structure. Later, cassiterite replacement of magnetite could be observed; (4) In the quartz-magnetite stage, large amounts of idiomorphic-hypidiomorphic magnetites occur. The ores have a massive structure. The magnetite granules form angles of 120° between each other (Figure 3j).

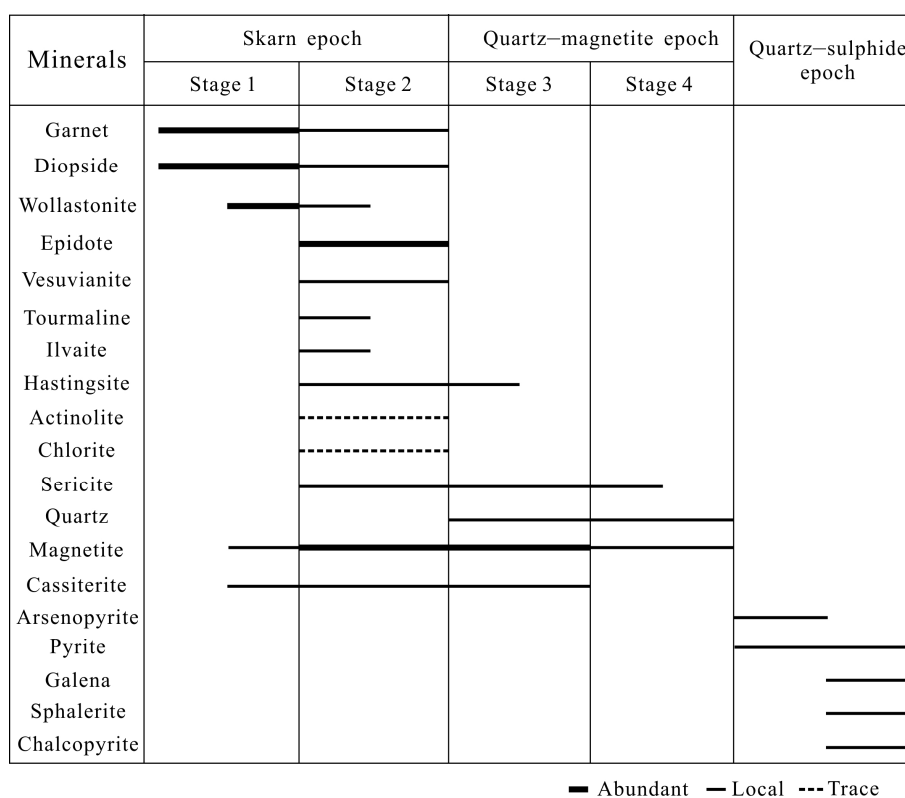


Figure 4. Paragenetic sequence of minerals from the Huanggangliang Sn-Fe deposit.

#### 4. Sampling and Analyses

##### 4.1. Sample Sites

Ore samples were collected from boreholes and outcrops of the no. 2–no. 22 orebodies in the the Huanggangliang deposit. The locations and types of samples are listed in Table 1.

**Table 1.** Location and descriptions of samples from the Huanggangliang deposit.

| Sample No.         | Location                                                                  | Ore Types                   | Stage | Description                                                        |
|--------------------|---------------------------------------------------------------------------|-----------------------------|-------|--------------------------------------------------------------------|
| HGL-153<br>ZK581-7 | 1400 m level, no. 2-3 mineralized veins<br>133 m, drill hole ZK1401/587-7 | Disseminated magnetite ores | I     | Garnet, diopside, magnetite,<br>cassiterite                        |
| HGL-149<br>HGL-313 | 1337.5 m level, no. 16-2 veins<br>1550 m level, no.4 mineralized vein     | Disseminated magnetite ores | II    | Epidote, chlorite, gokumite,<br>hastingsite magnetite, cassiterite |
| HGL-220            | 1187.5 m level, no. 22 mineralized vein                                   | Massive magnetite ores      | III   | Quartz, magnetite, cassiterite                                     |
| HGL-54             | 1350 m level, no. 12 mineralized vein                                     | Massive magnetite ores      | IV    | Quartz, magnetite                                                  |

#### 4.2. Electron-Probe Microanalyses

The chemical composition of magnetite was analyzed using a SHIMADZU EPMA-1720 electron microprobe (SHIMADZU, Tokyo, Japan) equipped with four wave length dispersive spectrometers and energy-dispersive system at the Key Laboratory of Metallogenic Prediction of Nonferrous Metals and Geological Environment Monitoring, Ministry of Education, China. Operating conditions include an accelerating voltage of 15 kV, electron beam current of 10 nA, and beam diameter of 1 to 2  $\mu\text{m}$ . All data were corrected using the atomic number-absorption-fluorescence (ZAF) procedure.

#### 4.3. LA-ICP-MS Trace Element Microscopic In Situ Analysis

LA-ICP-MS trace element microscopic in situ analysis was conducted at the Nanjing Jupu Analysis Technology Co., Ltd. (Nanjing, China) The LA-ICP-MS analysis system consists of the Analyze Excite 193 nm ArF Laser Ablation System (LA) made in the USA, and the Agilent 7700 $\times$  induced polarization plasma mass spectrum (ICP-MS) made in Japan. During laser ablation, the high intensity ultraviolet beams generated by the laser generator are focused on the sulfide through the homogenized light path. The energy density is 4.0 J/cm<sup>2</sup>. The beam diameter is 40  $\mu\text{m}$ . Each analysis includes a background acquisition of approximately 20 s (gas blank) followed by 40 s data acquisition from the sample. The frequency is 7.0 Hz. The ICPMS-DataCal software (China University of Geosciences, Wuhan, China) is adopted for offline processing of the analysis data and includes selection of the sample and blank signal, equipment sensitivity drift calibration, and element content calculation. The LA-ICP-MS analytical results are listed in Table 2. In-situ LA-ICP-MS analysis on the trace elements of the magnetite shows that the Al, Mg, Mn, Ti, Zr, Pb, Zn, Ni, Co, V, and Cr contents of the four types of magnetite exceed the detection limit, and that the Sc, Cu, Nb, Ta, and Na contents of some samples approach or slightly exceed the detection limit (Figure 5).

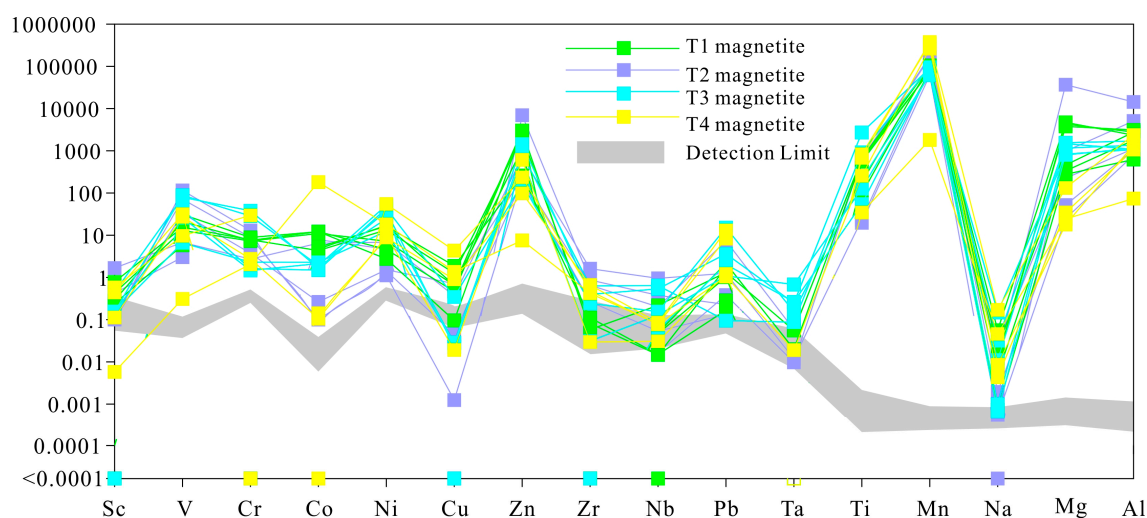


**Figure 5.** LA-ICP-MS analytical results from magnetite of Huanggangliang deposit, which are compared to the instrument limits of detection.

**Table 2.** Analytical results of selected ores from the Huanggangliang deposit.

| Sample No.   | Stage | Al <sub>2</sub> O <sub>3</sub> | SiO <sub>2</sub> | MnO  | FeO   | Mg   | Sc   | Ti   | V    | Cr   | Co   | Ni   | Zn   | Zr   | Nb   | Ta   | Pb   |
|--------------|-------|--------------------------------|------------------|------|-------|------|------|------|------|------|------|------|------|------|------|------|------|
|              |       | wt %                           | wt %             | wt % | wt %  | ppm  |
| HGL-153      | I     | 0.96                           | 0.24             | 0.68 | 92.97 | 980  | 0.42 | 20   | 3.0  | 0.01 | 7.9  | 4.7  | 6960 | 0.87 | 0.38 | 0    | 0.23 |
| HGL-153      |       | 2.71                           | 13.49            | 0.41 | 74.59 | 37   | 1.7  | 24   | 6.8  | 2.7  | 6.5  | 6.8  | 720  | 1.6  | 0.95 | 0.01 | 1.3  |
| zk1401/581-7 |       | 0.21                           | 0.38             | 0.22 | 96.11 | 220  | 0.1  | 610  | 33   | 3.8  | 0.26 | 1.5  | 230  | 0.65 | 0.2  | 0.06 | 7.4  |
| zk1401/581-7 |       | 0.15                           | 0.1              | 0.23 | 96.65 | 25   | 0.1  | 600  | 120  | 13   | 0.01 | 1.4  | 200  | 0.27 | 0.05 | 0    | 0.13 |
| zk1401/581-7 |       | 0.2                            | 0.19             | 0.24 | 96.49 | 52   | 0.11 | 650  | 71   | 8.9  | 0.1  | 1.1  | 22   | 0    | 0.02 | 0.01 | 0.38 |
| zk1401/581-7 |       | 0.85                           | 2.88             | 0.36 | 91.36 | 7600 | 0.48 | 380  | 46   | 5.7  | 2.9  | 3.1  | 1670 | 0.68 | 0.32 | 0.02 | 1.9  |
| HGL-149      | II    | 0.34                           | 0.05             | 0.16 | 96.39 | 340  | 0.43 | 550  | 13   | 0.01 | 4.7  | 17   | 1130 | 0    | 0    | 0    | 2.2  |
| HGL-149      |       | 0.52                           | 0.14             | 0.2  | 95.95 | 460  | 0.78 | 610  | 15   | 7.8  | 4.3  | 13   | 2140 | 0.08 | 0.01 | 0    | 1.1  |
| HGL-149      |       | 0.12                           | 0.11             | 0.19 | 96.49 | 280  | 0.24 | 96   | 5.8  | 0.01 | 5.2  | 16   | 260  | 0.11 | 0.01 | 0    | 15   |
| HGL-313      |       | 0.59                           | 0.04             | 1.47 | 93.82 | 3780 | 0.29 | 660  | 21   | 7.6  | 12   | 4.6  | 2960 | 0.06 | 0.22 | 0.06 | 2.03 |
| HGL-313      |       | 0.53                           | 0.05             | 1.5  | 93.98 | 4260 | 0    | 180  | 13   | 7.3  | 11   | 7.2  | 3020 | 0    | 0.05 | 0    | 3.6  |
| HGL-313      |       | 0.44                           | 0.07             | 3.53 | 92.02 | 4720 | 0    | 610  | 31   | 8.8  | 12   | 2.8  | 3000 | 0    | 0.05 | 0.02 | 0.1  |
| HGL-313      |       | 0.42                           | 0.08             | 1.18 | 94.77 | 2300 | 0.29 | 450  | 17   | 5.2  | 8.3  | 10.3 | 2080 | 0.04 | 0.06 | 0.01 | 4.0  |
| HGL-220      | III   | 0.26                           | 0.11             | 0.14 | 96.31 | 18   | 0.44 | 830  | 32   | 0.01 | 0.04 | 9.8  | 610  | 0.03 | 0.03 | 0    | 13   |
| HGL-220      |       | 0.2                            | 0.38             | 0.09 | 96.4  | 35   | 0.59 | 260  | 9.8  | 30   | 1    | 55   | 240  | 0.48 | 0.08 | 0.02 | 8.3  |
| HGL-220      |       | 0.45                           | 1.02             | 0.08 | 95.19 | 130  | 0.11 | 680  | 27   | 2.8  | 0.11 | 8.8  | 99   | 0.66 | 0.09 | 0    | 1.2  |
| HGL-220      |       | 0.01                           | 0.2              | 0    | 93.63 | 24   | 0.01 | 35   | 0.31 | 2.0  | 180  | 18   | 7.5  | 0.42 | 0.08 | 0    | 1.1  |
| HGL-220      |       | 0.23                           | 0.43             | 0.08 | 95.38 | 52   | 0.29 | 450  | 17   | 8.6  | 46   | 23   | 240  | 0.4  | 0.07 | 0    | 5.9  |
| HGL-54       | IV    | 0.2                            | 0.45             | 0.31 | 96    | 840  | 0.15 | 130  | 26   | 1.5  | 2.1  | 25   | 650  | 0.03 | 0.13 | 0.68 | 0.29 |
| HGL-54       |       | 0.22                           | 0.81             | 0.2  | 95.76 | 800  | 0    | 210  | 40   | 1.6  | 1.5  | 43   | 170  | 0.24 | 0.16 | 0.15 | 1.7  |
| HGL-54       |       | 0.2                            | 0.31             | 0.6  | 95.81 | 1480 | 0.16 | 55   | 6.6  | 2.3  | 2.3  | 12   | 860  | 0    | 0.06 | 0.26 | 0.17 |
| HGL-54       |       | 0.32                           | 0.42             | 0.55 | 94.93 | 1550 | 0.45 | 2710 | 79   | 38   | 1.7  | 37   | 1440 | 0.4  | 0.54 | 0.25 | 1.3  |
| HGL-54       |       | 0.26                           | 0.43             | 0.38 | 95.6  | 1160 | 0.15 | 920  | 88   | 29   | 1.9  | 51   | 860  | 0.63 | 0.64 | 0.09 | 1.0  |
| HGL-54       |       | 0.24                           | 0.48             | 0.41 | 95.62 | 1160 | 0.18 | 800  | 48   | 14   | 1.9  | 34   | 800  | 0.26 | 0.3  | 0.29 | 0.9  |

The concentration of Fe, Al, Si, and Mg are from EPMA.

The two types of disseminated magnetite show big differences in geochemical characteristics. T1 magnetite shows positive correlations in Mn vs. Mg, Al vs. Mg, Si vs. Mg, Co vs. Mg, Ni vs. Co, and V vs. Cr diagrams (Figure 6), while it is not strongly linked with Zn or Mg. Compared with T2 magnetite, T1 magnetite has extremely high Al content (2.71 wt %). Similar to T1 magnetite, T2 magnetite shows positive correlations in Mn vs. Mg, Al vs. Mg, Co vs. Mg, and V vs. Cr diagrams, and is not strongly linked with Cr or Ti contents. However, the Si vs. Mg and Ni vs. Co diagrams demonstrate a clear negative correlation and extremely high Mn content (3.53 wt %) (Figure 6).

Similar to the two types of disseminated or banded magnetite ores (T1 magnetite and T2 magnetite), the massive magnetites (T3 magnetite and T4 magnetite) show positive correlation in the Mn vs. Mg and Al vs. Mg diagram (Figure 6), while other minerals show different geochemical characteristics. Besides, the two types of magnetites also show different geochemical features with each other. Similar to T3 magnetite, T4 magnetite shows a negative correlation in the Ni vs. Co diagram. However, T4 magnetite shows a positive correlation in the Zn vs. Mg, Co vs. Mg, V vs. Cr, and Cr vs. Ti diagram, while it shows clear negative correlation in the Si vs. Mg diagram and extremely high Ti content (54.76–2711.24 ppm) (Figure 6).

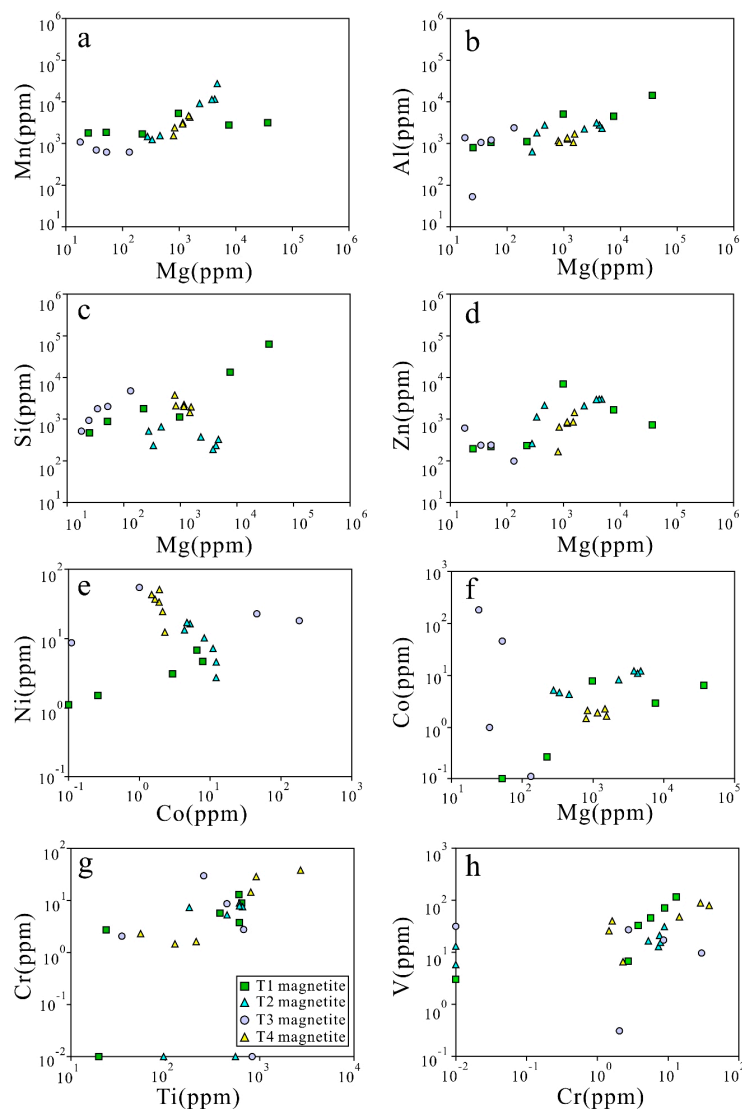


**Figure 6.** Binary diagrams of (a) Mn vs. Mg, (b) Al vs. Mg, (c) Si vs. Mg, (d) Zn vs. Mg, (e) Ni vs. Co, (f) Co vs. Mg, (g) Cr vs. Ti, and (h) V vs. Cr for the Huanggangliang disseminated- and massive-magnetite ores.

## 5. Discussion

### 5.1. Petrography and Genesis of the Huanggangliang Magnetite

The T1 and T2 magnetites were formed during the garnet–diopside–magnetite (T1) stage and the epidote–idocrase–cassiterite–magnetite (T2) stage during the skarn period (Figure 3). Both coexist with the alteration minerals in the typical skarn-type deposits (i.e., garnet, diopside, idocrase, epidote, hastingsite). The T1 magnetites mainly occur within the fissures between the diopsides and the zoned garnets or replace the early diopsides and garnets and then are later replaced by cassiterite. The T2 magnetites replace the earlier epidotes and diopsides and are later replaced by cassiterites (Figure 3). The massive T3 magnetite ores are cemented with the magnetite breccias that were formed during the skarn period (i.e., T1 and T2 magnetites) (Figure 3c,d). The T3 magnetite coexist with cassiterite and a small amount of quartz and replace the earlier hastingsite (Figure 3). The T4 magnetite-bearing ores mainly occur in massive structures. The T4 magnetite is cross-cut by later sulfides, indicating that the magnetite mineralization likely predated sulfides. In addition, the T4 magnetite shows a good crystal shape. The idiomorphic magnetite granules form angles of  $120^\circ$  between each other. Currently, two models could be adopted to explain the triple junction texture of the T4 magnetite: (1) high-temperature annealing in a closed system (i.e., magmatic magnetite, [43]), and (2) fluid-assisted recrystallization/replacement in an open system (i.e., quartz, [44,45]). The low Ni and Cr contents and relatively high and stable Fe contents of the T4 magnetite indicate that it does not belong to magmatic magnetite [41]. Hydrothermal magnetite bears relatively low contents of Ti (<2300 ppm) compared with magmatic magnetite. The Ti and V contents of the magnetites of the area fall into the ranges of 19.69–918.99 ppm (with only one extremely high value, 2711.24 ppm) and 0.31–115.18 ppm, respectively. In addition, fluid inclusion studies of garnet and cassiterite in Huanggangliang deposit demonstrate that the temperature of the skarn period and magnetite-quartz period was below  $400^\circ\text{C}$  [16,19,20]. The fluid temperature should not belong to the high-temperature annealing system [40]. The polymetallic sulfide veins within the crack-seal textures that represent open space filling are common in the massive magnetite, suggesting a local extensional tectonic regime [46]. This indicates that the triple junction texture in the massive magnetites were probably derived from fluid-assisted recrystallization/replacement in an open system.

Among the various magnetite ore types at Huanggangliang we distinguished the Ni vs. Cr and V/Ti vs. Fe diagrams (Figure 7a,b). Thus the Huanggangliang magnetite (banded-, disseminated-, and massive magnetite ores) are hydrothermal. The depletions of Ti (<0.09 wt %), Al (0.008–1.731 wt %) and Zr (<1.610 ppm) in magnetite also suggest hydrothermal magnetite affinities [28,30,32,47].

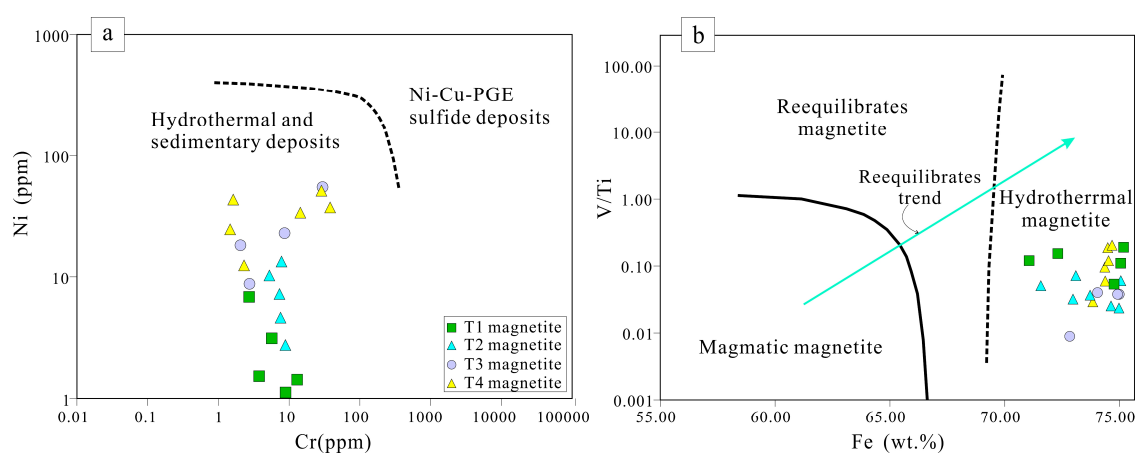


**Figure 7.** Binary diagrams of (a) Ni vs. Cr (after Reference [30]), and (b) V/Ti vs. Fe (after Reference [42]) for the Huanggangliang magnetite from the different ore types.

## 5.2. Controlling Factors for Magnetite Compositions

Factors affecting the trace element compositions of magnetite in the hydrothermal fluids include fluid compositions, host rock compositions, coexisting minerals, temperature, and oxygen fugacity ( $f_{O_2}$ ) [28,30,31,48,49].

### 5.2.1. Coexisting Minerals, Fluid and Host Rock Compositions

Micro-inclusions in magnetite can influence the bulk magnetite geochemistry detected (Table 2). The few anomalously high Si, Al, Mn, Mg, Ti, and Zn magnetite grains may point to the presence of Mn-bearing phases, Ti-bearing phases, sphalerite inclusions, and/or silicate (Figure 8).

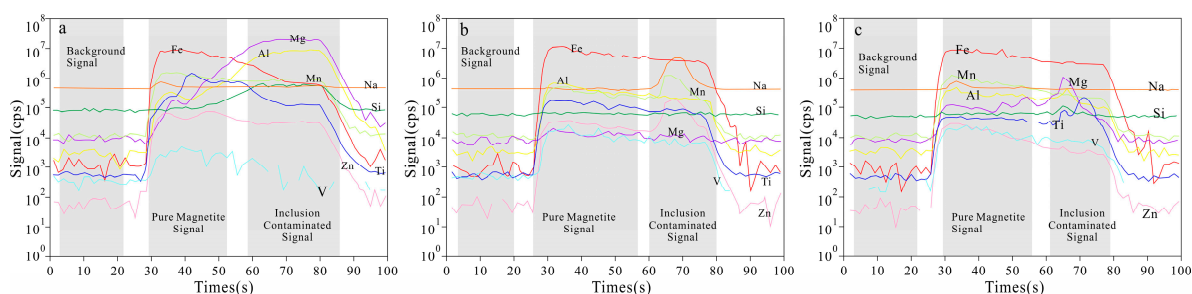


**Figure 8.** Time-resolved analytical signals of a LA-ICP-MS analysis from disseminated- and massive-magnetite ores. (a) Disseminated magnetite ores (T2); (b) Massive magnetite ores (T3); (c) Massive magnetite ores (T4). Suspected fluid inclusions are characterized by high Si, Al, Mn, Mg, Ti, and Zn intensities (cps counts per second).

Fluid-rock interactions enabled the hydrothermal magnetite to inherit some geochemical features of the altered wall rock or altered minerals [30,48]. In Figure 9, the T1 and T2 magnetites are formed during the skarn period. Both might be the products of the same metallogenic fluid system. The T1 magnetite was formed during the garnet–diopside–cassiterite–magnetite stage, which marked the beginning of metallogenesis in the area. The Co/Ni ratio varies in the range of 0.01–1.67, averaging 0.58. The sample points fall into the range between magnetite-forming fluids (low Co/Ni = 0.01, [50,51]) and the Permian Dashizhai marine sediments and skarn, suggesting that the formation of the T1 magnetite was due to the fluid-rock interactions between the magnetite-forming fluids, Permian Dashizhai marine sediments and the early skarn minerals (such as garnet and diopside). The Co/Ni values of the T2 magnetites vary in the range of 0.27–4.41, averaging 1.58, which is higher than those of the T1 magnetite. In the diagram (Figure 9), the sample points fall into the skarn range, suggesting that the formation of the T2 magnetite occurred simultaneously with petrogenesis (i.e., epidote–diopside–wollastonite skarn). The T3 and T4 magnetites were formed during the quartz-magnetite period. The T3 magnetite was formed during the early stage of the quartz-magnetite period and has a wide range of Co/Ni ratios (0.01–9.56, averaging 2.50). The sample points are distributed over a wide range, with a few sample points falling out of the range of skarn and the Permian Dashizhai Formation marine sediments (Figure 9). Its formation might be the result of interactions between the magnetite-forming fluids and the preexisting skarn, as well as the Permian Dashizhai marine sediments and other strata. The T4 magnetite was formed during the late stage of the quartz-magnetite metallogenic period. The Co/Ni ratios vary over the range of 0.04–0.18, averaging 0.08. The sample points are relatively concentrated in the range of magnetite-forming fluids and skarn (Figure 9), suggesting that its formation is related to the fluid-rock interaction between the magnetite-forming fluids and the preexisting skarn.

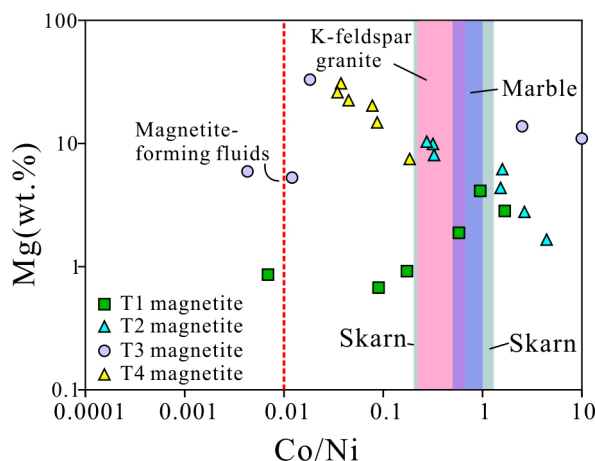


**Figure 9.** Binary diagrams of Mg (wt %) vs. Co/Ni for the Huanggangliang magnetite from the different ore types.

### 5.2.2. Temperature and Oxygen Fugacity ( $f_{O_2}$ )

Temperature could affect the trace element composition of the hydrothermal magnetite [30,31]. Experimental studies indicated that Zn and Mn would be the priorities for entering magnetite in the condition of lower temperatures [52]. In the Huanggangliang deposit, the Zn contents in the four types of magnetite are 1560.96–4661.93 ppm, avg. 3169.99 ppm in T1; 1216.63–27364.18 ppm, avg. 9101.14 ppm in T2; 1673.99–5301.95 ppm, avg. 2768.82 ppm in T3; and 9.93–1093.55 ppm, avg. 593.50 ppm in T4. The Mn contents are T1(166.14–1444.24 ppm, avg. 794.72 ppm), T2 (259.45–3016.06 ppm, avg. 2085.73 ppm), T3 (195.33–6958.99 ppm, avg. 1665.85 ppm), and T4 (7.54–611.12 ppm, avg. 238.45 ppm). The Mn and Zn contents of the four types of magnetites differ from each other, which might have been the result of different temperatures during the precipitation of magnetites. However, fluid inclusion studies of the garnet and cassiterite demonstrate that the formation temperatures of the four types of fluid inclusions vary over the range of 349 to 432 °C [16], showing a small range of variation. The difference in Zn and Mn contents might be due to the Mn-bearing and Zn-bearing inclusions (Figure 7). The titanium within the magnetite is generally believed to be positively related to its formation temperature [29,32,53]. In the (Al + Mn) vs. (Ti + V) diagram (Figure 10a), the magnetites of the different Huanggangliang ore types show similar distribution patterns, suggesting that the temperature had little effect on the compositions of the magnetites.

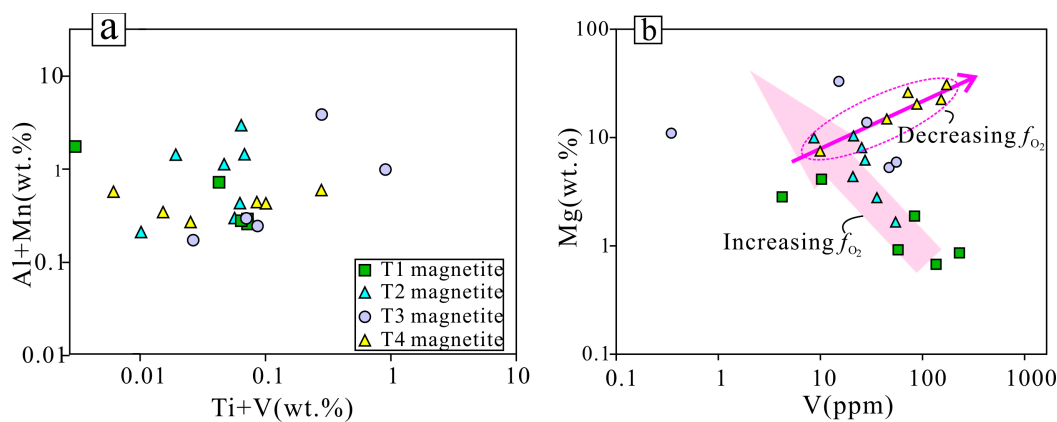


**Figure 10.** (a) Al + Mn vs. Ti + V correlation diagram; (b) Mg vs. V plot.

Vanadium exists mostly in the form of (+3, +4, +5) in fluids. Only  $V^{3+}$  could enter the crystal cube of magnetite [31,38,54], i.e., the increase in vanadium content in magnetite represents the decrease in oxygen fugacity [38,41,55]. In Figure 10b, the variation range of V tends to become lower from T1 to T3 magnetite, suggesting that the oxygen fugacity of the metallogenic fluids increased as the metallogenesis proceeded. The V content in the T4 magnetite tends to increase, indicating that the oxygen fugacity of the metallogenic fluids tends to decrease. As the metallogenesis proceeded to the quartz-magnetite stage (Stage 4), the oxygen fugacity of the metallogenic fluid system weakened, and the reduction of the system became stronger. The metallogenesis tended to transition toward the quartz-sulfide period.

### 5.3. Indications for the Genesis of the Deposit

The stratiform and lenticular ore bodies of the Huanggangliang Sn-Fe deposit are clearly associated with the skarn belt in the contact zone between the Yanshanian alkali granite and the wall rock (Figure 2). The LA-ICP-MS zircon ages of the Huanggangliang k-feldspar granite are in the range of 136.7–139.9 Ma [6,9]. The corresponding molybdenite (quartz-sulfide period) has Re-Os isochron ages in the range of 135.3–134.9 Ma [7,9]. The metallogenic age of the Huanggangliang deposit is similar to the age of the rock body and is remarkably different from the age of the ore-hosting Permian Zhesi Formation strata. Therefore, the deposit is unlikely to be a sedimentary-exhalative deposit. Magnetite is a key ore mineral in Fe-dominated deposits, including banded iron formation (BIF), Kiruna-type magmatic Fe-Ti oxide, and Fe skarn deposits [28,32], as well as in other types of hydrothermal deposits such as iron oxide-copper-gold (IOCG) and porphyry Cu-Au systems [56,57], which are mostly sub-economic. The high Ni/Cr ratios of the four types of magnetite are all similar to the magnetite of the typical magmatic hydrothermal/hydrothermal deposits (i.e., skarn, IOCG, porphyry-type and Ag-Pb-Zn vein type deposits) (Figure 11a). Therefore, it is difficult to precisely identify the genesis of the deposit based on the Ni/Cr ratios within the four types of magnetites. The relatively low Ti + V (wt %) content, Ni/(Cr + Mn) ratio and high Al + Mn (wt %) content (Figure 11b,c) all demonstrate that the four types of magnetites in the deposit share similar features with skarn deposits, which are remarkably different from those of IOCG, porphyry-type and BIF deposits.

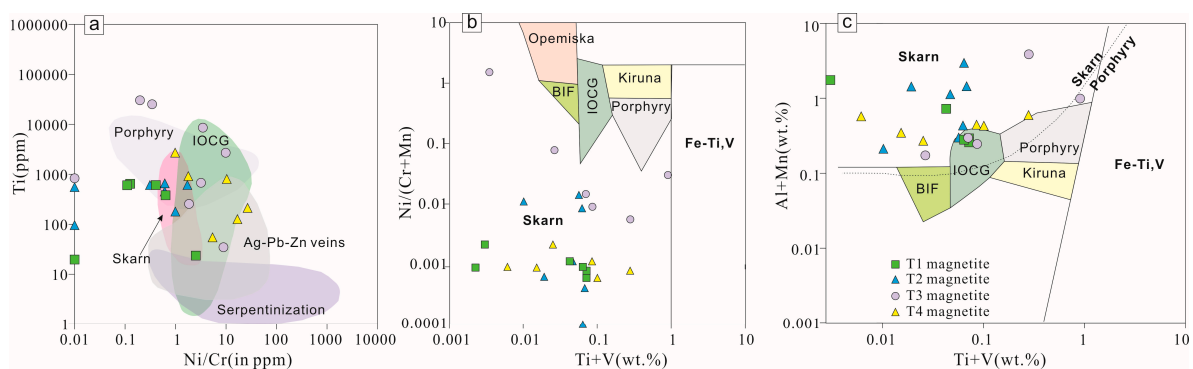


**Figure 11.** Magnetite discrimination diagrams (a) Ti vs. Ni/Cr (after Reference [30]); (b) Ni/(Cr + Mn) vs. (Ti + V) (after Reference [28]); (c) (Ti + V) vs. (Al + Mn) (after Reference [28]).

In the multi-element diagram (Figure 12), the four types of magnetites share similar distribution patterns, which suggests similar sources. The four types of magnetites show different degrees of depletion in Zr, Nb, Mg, and Co, and slight enrichment of Mn and Zn. These features are similar to those of the magnetites in the skarn and IOCG deposits, while they are different from the magnetite of BIF-type deposits. However, the enrichment of Al and depletion of Sc, V, Ni, and Cr are different from the features of the IOCG-type deposit. In addition, the epidotization, tourmalinization, and sericitization of the deposit all occurred during the metallogenic period. In the case of IOCG deposits, these types of alterations mostly occur before the metallogenic period [56,58,59]. To summarize, we

believe that the Huanggangliang deposit is a skarn-type Sn-Fe deposit whose genesis is related to Yanshanian medium-acidic magmatic activities.

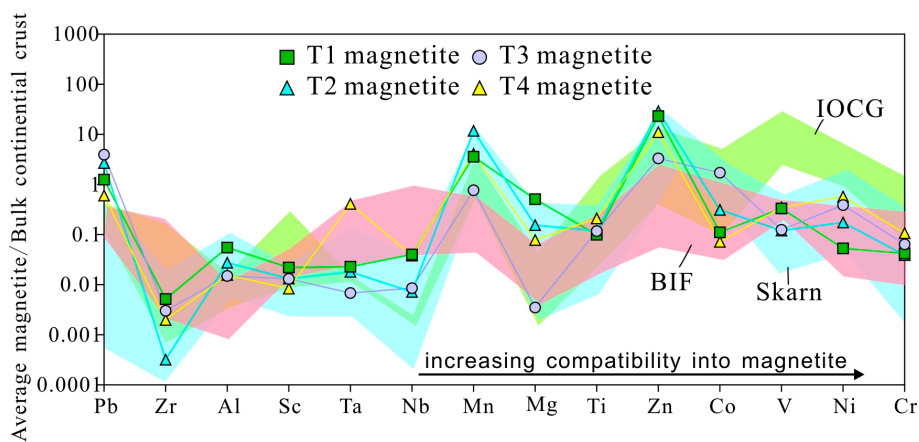


**Figure 12.** Multi-element diagram for the Heijianshan magnetite, normalized to bulk continental crust. Data for IOCG from the Ernest Henry deposit [30], BIF from the Sokoman Fe formation [60], skarn from the Tengtie skarn Fe [61], and Vegas Peledas calcic skarn Fe [30] deposits are shown for comparison (normalization values from Reference [62]).

## 6. Conclusions

- (1) Petrographic characteristics and geochemical parameters of magnetite suggest that the four types of magnetites all belong to hydrothermal magnetite.
- (2) Compositions of the ore fluids and host rocks, formation of coexisting minerals, and other physical and chemical parameters (such as  $fO_2$ ) may have variably influenced the magnetite geochemistry in the different Huanggangliang ore types, with fluid compositions and  $fO_2$  probably playing the most important role.
- (3) Geological characteristics, micro-structural features, and trace element traits of the Huanggangliang Sn-Fe deposit indicate that the deposit is a skarn-type Sn-Fe deposit associated with Yanshanian medium-acidic magmatic activities.

**Author Contributions:** C.W., Y.S., and Z.L. conceived and designed the experiments; C.W. performed the experiments; X.Z. and J.D. helped editing and improved English wording and language style; all authors wrote the paper.

**Acknowledgments:** This work was supported by the Innovation-driven Plan of Central South University (Project 1053320180985) and the National Natural Science Foundation of China (Grant no. 41702078).

**Conflicts of Interest:** The authors declare no conflict of interest.

## References

1. Rui, Z.Y.; Shi, L.D.; Fang, R.Y. *Geology and Nonferrous Metallic Deposits in the Northern Margin of the North China Landmass and Its Adjacent Area*; Geological Publishing House: Beijing, China, 1994; pp. 1–476. (In Chinese)
2. Liu, J.M.; Zhang, R.; Zhang, Q.H. The regional metallogeny of Dahingganling, China. *Earth Sci. Front.* **2004**, *11*, 269–277. (In Chinese)
3. Wang, C.Y. Lead-Zinc Polymetallic Metallogenic Series and Prospecting Direction of Huanggangliang–Ganzhuermiao Metallogenic Belt, Inner Mongolia. Ph.D. Thesis, Jilin University, Jilin, China, 2014. (In Chinese)
4. Zhang, D.H. Geological setting and ore types of the Huanggang–Ganzhuermiao tin, silver and polymetallic ore zone in eastern Inner Mongolia. *Bull. Inst. Miner. Depos.* **1989**, *1*, 41–54. (In Chinese)
5. Li, H.N.; Duan, G.Z. Metallogenic model of Huanggang iron tin polymetallic deposit. *Glob. Geol.* **1988**, *7*, 17–28. (In Chinese)

6. Zhou, Z.H.; Lu, L.S.; Wang, A.S. Deep source characteristics and tectonic–magmatic evolution of granites in the Huanggang Sn–Fe deposit, Inner Mongolia: Constraint from Sr–Nd–Pb–Hf multiple isotopes. *Geol. Sci. Technol. Inf.* **2011**, *30*, 1–14. (In Chinese)
7. Zhou, Z.H. *Geology and Geochemistry of Huanggang Sn–Fe Deposit, Inner Mongolia*; Chinese Academy of Geological Sciences: Beijing, China, 2011. (In Chinese)
8. Zhao, H.; Li, S.; Wang, T.; Wang, W.Z.; Jiao, Y.Y. Age, petrogenesis and tectonic implications of the Early Cretaceous magmatism in the Huanggangliang area, southern Dahinggan Mountains. *Geol. Bull. China* **2015**, *34*, 2203–2218. (In Chinese)
9. Zhai, D.G.; Liu, J.J.; Yang, Y.Q.; Wang, J.P.; Ding, L.; Liu, X.W.; Zhang, M.; Yao, M.J.; Su, L.; Zhang, H.Y. Petrogenetic and metallogenic ages and tectonic setting of the Huanggangliang Fe–Sn deposit Inner Mongolia. *Acta Petrol. Mineral.* **2012**, *32*, 513–523. (In Chinese)
10. Feng, J.Z.; Ai, X.; Wu, Y.B. Geological characteristics and metallogenic model in Huanggangliang–Mengentaolegai metallogenic belt, Inner Mongolia. *Liaoning Geol.* **1993**, *3*, 244–253. (In Chinese)
11. Niu, H.L. Geological Characteristics of Huanggangshan Sn–Polymetallic Ore Deposit in Keshiketeng Banner, Inner Mongolia. Master’s Thesis, Shijiazhuang University of Economics, Shijiazhuang, China, 2013. (In Chinese)
12. Jiang, X.S. Mineralogical properties of magnetite from Huanggang iron–tin ore deposit and its significance to the ore genesis. *Bull. Shenyang Inst. Geol. Miner. Res. Chin. Acad. Geol. Sci.* **1981**, *2*, 84–93. (In Chinese)
13. Zeng, S.H. The existing form of tin in magnetite in the iron–tin deposit from Huanggang, Neimenggu. *Mineral. Petrol.* **1992**, *12*, 23–35. (In Chinese)
14. Xiao, C.D.; Liu, X.W. REE geochemistry and origin of skarn garnets from eastern Inner Mongolia. *Geol. China* **2002**, *3*, 311–316. (In Chinese)
15. Wu, S.; Gu, X.P.; Feng, Y.Z.; Jiang, M.T.; Zhao, R.C. Composition typomorphic characteristics of the cassiterite in Huanggang Sn–Fe polymetallic deposit, Inner Mongolia. *South. Metals* **2016**, *210*, 40–43. (In Chinese)
16. Xu, Z.B.; Shao, Y.J.; Yang, Z.A.; Liu, Z.F.; Wang, W.X.; Ren, X.M. LA–ICP–MS analysis of elements in sphalerite from the Huanggangliang Fe–Sn, Inner, and its implication. *Acta Petrol. Mineral.* **2017**, *36*, 360–370. (In Chinese)
17. Zhai, D.G.; Liu, J.J.; Zhang, H.Y.; Yao, M.J.; Wang, J.P.; Yang, Y.Q. S–Pb isotopic geochemistry, U–Pb and Re–Os geochronology of the Huanggangliang Fe–Sn deposit, Inner Mongolia, NE China. *Ore Geol. Rev.* **2014**, *59*, 109–122. [[CrossRef](#)]
18. Yao, M.J.; Cao, Y.; Liu, J.J.; Zhai, D.G. Isotope age of Re–Os in molybdenite and genetic implication of Huanggangliang Fe–Sn deposit in Inner Mongolia. *Min. Explor.* **2016**, *7*, 399–403. (In Chinese)
19. Wang, L.J.; Hidehiko, S.; Wang, J.B.; Wang, Y.W. Ore-forming fluid and mineralization of the Huanggangliang skarn Fe–Sn deposit, Inner Mongolia. *Sci. China D Ser.* **2001**, *31*, 553–562.
20. Zhou, Z.H.; Wang, A.S.; Li, T. Fluid inclusion characteristics and metallogenic mechanism of Huanggang Sn–Fe deposit in Inner Mongolia. *Miner. Depos.* **2011**, *30*, 867–889. (In Chinese)
21. Wang, C.M.; Zhang, S.T.; Deng, J.; Liu, J.M. The exhalative genesis of the stratabound skarn in the Huanggangliang Sn–Fe polymetallic deposit of Inner Mongolia. *Acta Petrol. Mineral.* **2007**, *5*, 409–417. (In Chinese)
22. Liu, Z.; Lu, X.B.; Mei, W. Sulfur–lead–oxygen isotope compositions of the Huanggang skarn Fe–Sn deposit, Inner Mongolia: Implication for the sources of ore-forming materials. *Mineral. Petrol.* **2013**, *3*, 30–37. (In Chinese)
23. Yang, G.F. Geological formation and ore-controlling process of Permian system in the southern part of Dahingganling, Inner Mongolia. *Miner. Resour. Geol.* **1996**, *10*, 120–125. (In Chinese)
24. Wang, L.J.; Wang, J.B.; Wang, Y.W.; Shimazaki, H. REE geochemistry of the Huanggangliang skarn Fe–Sn deposit, Inner Mongolia. *Acta Petrol. Sin.* **2002**, *4*, 575–584. (In Chinese)
25. Xu, J.J.; Lai, Y. Zircon U–Pb age of granites and its geological significance in Huanggang skarn Fe–Sn deposit, Inner Mongolia. *Acta Geol. Sin.* **2015**, *s1*, 46–47. (In Chinese)
26. Liu, J.; Ye, J.; Li, Y.; Chen, X.; Hang, R. A preliminary study on exhalative mineralization in Permian basins, the southern segment of the Da Hinggan Mountains, China—Case studies of Huanggang and Dajing deposits. *Resour. Geol.* **2001**, *51*, 345–358. [[CrossRef](#)]

27. Ye, J.; Liu, J.M.; Zhang, A.L.; Zhang, R.B. Petrological evidence for exhalative mineralization: Case studies of Huanggang and Da jing deposits in the the southern segment of the Dahinggan Mountains, China. *Acta Petrol. Sin.* **2002**, *4*, 585–592. (In Chinese)
28. Dupuis, C.; Beaudoin, G. Discriminant diagrams for iron oxide trace element fingerprinting of mineral deposit types. *Miner. Depos.* **2011**, *46*, 319–335. [[CrossRef](#)]
29. Dare, S.A.; Barnes, S.J.; Beaudoin, G. Variation in trace element content of magnetite crystallized from a fractionating sulfide liquid, Sudbury, Canada: Implications for provenance discrimination. *Geochim. Cosmochim. Acta* **2012**, *88*, 27–50. [[CrossRef](#)]
30. Dare, S.A.; Barnes, S.J.; Beaudoin, G.; Méric, J.; Boutroy, E.; Potvin, D.C. Trace elements in magnetite as petrogenetic indicators. *Miner. Depos.* **2014**, *49*, 785–796. [[CrossRef](#)]
31. Nadoll, P.; Angerer, T.; Mauk, J.L.; French, D.; Walshe, J. The chemistry of hydrothermal magnetite: A review. *Ore Geol. Rev.* **2014**, *61*, 1–32. [[CrossRef](#)]
32. Nadoll, P.; Mauk, J.L.; Hayes, T.S.; Koenig, A.E.; Box, S.E. Geochemistry of magnetite from hydrothermal ore deposits and host rocks of the Mesoproterozoic Belt Supergroup, United States. *Econ. Geol.* **2012**, *107*, 1275–1292. [[CrossRef](#)]
33. Buddington, A.F.; Lindsley, D.H. Iron-titanium oxide minerals and synthetic equivalents. *J. Petrol.* **1964**, *5*, 310–357. [[CrossRef](#)]
34. Nash, W.P.; Crecraft, H.R. Partition coefficients for trace elements in silicic magmas. *Geochim. Cosmochim. Acta* **1985**, *49*, 2309–2322. [[CrossRef](#)]
35. Lindsley, D.H. *Oxide Minerals: Petrologic and Magnetic Significance*, 1st ed.; Mineralogical Society of America: Washington, DC, USA, 1991; p. 25.
36. Harlov, D.E. Comparative Oxygen Barometry in Granulites, Bamble Sector, SE Norway. *J. Geol.* **1992**, *100*, 447–464. [[CrossRef](#)]
37. Harlov, D.E. Titaniferous magnetite-ilmenite thermometry and titaniferous magnetite-ilmenite-orthopyroxene-quartz oxygen barometry in granulite facies gneisses, Bamble Sector, SE Norway: Implications for the role of high-grade CO<sub>2</sub>-rich fluids during granulite. *Contrib. Mineral. Petrol.* **2000**, *139*, 180–197. [[CrossRef](#)]
38. Toplis, M.J.; Corgne, A. An experimental study of element partitioning between magnetite, clinopyroxene and iron-bearing silicate liquids with particular emphasis on vanadium. *Contrib. Mineral. Petrol.* **2002**, *144*, 22–37. [[CrossRef](#)]
39. Knipping, J.L.; Bilenker, L.D.; Simon, A.C.; Reich, M.; Barra, F.; Deditius, A.P.; Wälle, M.; Heinrich, C.A.; Holtz, F.; Munizaga, R. Trace elements in magnetite from massive iron oxide-apatite deposits indicate a combined formation by igneous and magmatic-hydrothermal processes. *Geochim. Cosmochim. Acta* **2015**, *171*, 15–38. [[CrossRef](#)]
40. Li, D.F.; Chen, H.Y.; Pete, H.; Zhang, L.; Sun, X.M.; Zheng, Y.; Xia, X.P.; Xiao, B.; Wang, C.M.; Fang, J. Trace element geochemistry of magnetite: Implications for ore genesis of the Talate skarn Pb-Zn (-Fe) deposit, Altay, NW China. *Ore Geol. Rev.* **2017**, in press. [[CrossRef](#)]
41. Zhao, L.D.; Chen, H.Y.; Zhang, L.; Li, D.F.; Zhang, W.F.; Wang, C.M.; Yang, J.T.; Yan, X.L. Magnetite geochemistry of the Heijianshan Fe-Cu (-Au) deposit in Eastern Tianshan: Metallogenic implications for submarine volcanic-hosted Fe-Cu deposits in NW China. *Ore Geol. Rev.* **2017**, in press. [[CrossRef](#)]
42. Wen, G.; Li, J.W.; Albert, H.; Hofstra, A.E.; Koenig, H.A.; Lowers, D.A. Hydrothermal reequilibration of igneous magnetite in altered granitic plutons and its implications for magnetite classification schemes: Insights from the Handan-Xingtai iron district, North China Craton. *Geochim. Cosmochim. Acta* **2017**, in press. [[CrossRef](#)]
43. Ciobanu, C.L.; Cook, N.J. Skarn textures and a case study: The Ocna de Fier-Dognecea orefield, Banat, Romania. *Ore Geol. Rev.* **2004**, *24*, 315–370. [[CrossRef](#)]
44. Hu, H.; Lentz, D.; Li, J.W.; Mccarron, T.; Zhao, X.F.; Hall, D. Reequilibration processes in magnetite from iron skarn deposits. *Econ. Geol.* **2015**, *110*, 1–8. [[CrossRef](#)]
45. Nakamura, M.; Watson, E.B. Experimental study of aqueous fluid infiltration into quartzite: Implications for the kinetics of fluid redistribution and grain growth driven by interfacial energy reduction. *Geofluids* **2001**, *1*, 73–89. [[CrossRef](#)]
46. Sibson, R.H.; Robert, F.; Poulsen, K.H. High-angle reverse faults, fluid-pressure cycling, and mesothermal gold-quartz deposits. *Geology* **1988**, *16*, 551–555. [[CrossRef](#)]

47. Ray, G.; Webster, I. Geology and chemistry of the low Ti magnetite-bearing Heff Cu-Au skarn and its associated plutonic rocks, Heffley Lake, south-central British Columbia. *Explor. Min. Geol.* **2007**, *16*, 159–186. [[CrossRef](#)]
48. Carew, M.J. Controls on Cu-Au Mineralization and Fe Oxide Metasomatism in the Eastern Fold Belt, NW Queensland, Australia. Ph.D. Thesis, James Cook University, Townsville, Australia, 2004.
49. Chen, H.Y.; Han, J.S. Study of magnetite: Problems and future. *Bull. Mineral. Petrol. Geochem.* **2015**, *34*, 724–730. (In Chinese)
50. Bajwah, Z.U.; Seccombe, P.K.; Offler, R. Trace element distribution Co: Ni ratios and genesis of the Big Cadia iron-copper deposit, New South Wales, Australia. *Miner. Depos.* **1987**, *22*, 292–300. [[CrossRef](#)]
51. Brill, B. Trace-element contents and partitioning of elements in ore minerals from CSA Cu-Pb-Zn deposit, Australia. *Can. Mineral.* **1979**, *27*, 263–273.
52. Ilton, E.S.; Eugster, H.P. Base metal exchange between magnetite and a chloride rich hydrothermal fluid. *Geochim. Cosmochim. Acta* **1989**, *53*, 291–301. [[CrossRef](#)]
53. Huang, X.W.; Zhou, M.F.; Qi, L.; Gao, J.F.; Wang, Y.W. Re-Os isotopic ages of pyrite and chemical composition of magnetite from the Cihai magmatic-hydrothermal Fe deposit, NW China. *Miner. Depos.* **2013**, *48*, 925–946. [[CrossRef](#)]
54. Bordage, A.; Balan, E.; de Villiers, J.P.; Cromarty, R.; Juhin, A.; Carvallo, C.; Calas, G.; Raju, P.V.; Glatzel, P.V. Oxidation state in Fe-Ti oxides by high-energy resolution fluorescence-detected X-ray absorption spectroscopy. *Phys. Chem. Miner.* **2011**, *38*, 449–458. [[CrossRef](#)]
55. Takeno, N. *Atlas of Eh-pH Diagrams*; Geological Survey of Japan Open File Report; National Institute of Advanced Industrial Science and Technology: Tokyo, Japan, 2005; p. 102.
56. Williams, P.J.; Barton, M.D.; Johnson, D.A.; Fontboté, L.; de Haller, A.; Mark, G.; Marschik, R. Iron oxide copper-gold deposits: Geology, space-time distribution, and possible modes of origin. *Econ. Geol.* **2005**, *371*–405.
57. Liang, H.Y.; Sun, W.; Su, W.C.; Zartman, R.E. Porphyry copper-gold mineralization at Yulong, China, promoted by decreasing redox potential during magnetite alteration. *Econ. Geol.* **2009**, *104*, 587–596. [[CrossRef](#)]
58. Chen, H.Y. External sulfur in IOCG mineralization: Implications on definition and classification of the IOCG clan. *Ore Geol. Rev.* **2013**, *51*, 74–78. [[CrossRef](#)]
59. Zhu, Q.Q.; Xie, G.Q.; Mao, J.W.; Li, W.; Li, Y.H.; Wang, J.; Zhang, P. Mineralogical and sulfur isotopic evidence for the incursion of evaporites in the Jinshandian skarn Fe deposit, Edong district, Eastern China. *J. Asian Earth Sci.* **2015**, *113*, 1253–1267. (In Chinese) [[CrossRef](#)]
60. Chung, D.; Zhou, M.F.; Gao, J.F.; Chen, W.T. In-situ LA-ICP-MS trace elemental analyses of magnetite: The late Palaeoproterozoic Sokoman Iron Formation in the Labrador Trough, Canada. *Ore Geol. Rev.* **2015**, *65*, 917–928. [[CrossRef](#)]
61. Zhao, W.W.; Zhou, M.F. In-situ LA-ICP-MS trace elemental analyses of magnetite: The Mesozoic Tengtie skarn Fe deposit in the Nanling Range, South China. *Ore Geol. Rev.* **2015**, *65*, 872–883. [[CrossRef](#)]
62. Rudnick, R.L.; Gao, S. Composition of the Continental Crust. *Treatise Geochem.* **2003**, *3*, 1–64.

